Electronic Supplementary Material (ESI) for Journal of Materials Chemistry A.
This journal is © The Royal Society of Chemistry 2023

Support Information

Effectively Enhanced Activity for Overall Water Splitting Through Interfacially-Strong P-Co-O Tetrahedral Coupling Interaction on CoO/CoP Heterostructure Hollow-Nanoneedles

Kai Chen[a+], Yonghua Cao[b+], Wenmeng Wang[a], Jinxiang Diao[c], Jaehong Park[a], Vandung Dao[a], Gyu-Cheol Kim[a], Yunteng Qu[d] and In-Hwan Lee[a]**

*[a]Department of Materials Science and Engineering, Korea University, Seoul 02841, Republic of Korea. *E-mail: ihlee@korea.ac.kr*

[b]School of Mechanical and Electrical Engineering, Henan Institute of Science and Technology, Xinxiang 453003, People's Republic of China.

[c]Aeronautical Polytechnic Institute, Xi'an 710089, People's Republic of China.

*[d]State Key Laboratory of Photoelectric Technology and Functional Materials, International Collaborative Center on Photoelectric Technology and Nano Functional Materials, Institute of Photonics and Photon-Technology, Northwest University, Xi'an, Shaanxi 710089, People's Republic of China. *E-mail: yuntengqu@nwu.edu.cn*

[+] Chen and Cao contributed equally to this work

1. Experimental Section

Chemicals: Cobalt(II) chloride hexahydrate ($CoCl_2·6H_2O$), urea ($CO(NH_2)_2$), dicyandiamide ($NH_2C(=NH)NHCN$), sodium hypophosphite hydrate ($NaH_2PO_2·_XH_2O$, ~95%), and Nafion (5 wt%) were purchased from SIGMA-ALDRICH. Furthermore, Ni foam was purchased from MTI corporation. All chemicals were not purified further.

Fabrication of the Co-precursor nanoneedles: The Co-precursor was produced by hydrothermal reaction. Typically, 6 mmol $CoCl_2·6H_2O$ and 12 mmol $CO(NH_2)_2$ were dissolved in 35 mL deionized (DI) water under magnetic stirring for 3 h until the solution clarification. After that, the mixed solution was transferred to a 50 mL hydrothermal autoclave and reacted at 120 °C for 6 h in the oven, and cooled down naturally. Finally, Co-precursor was received by extraction using a centrifuge with DI-water and ethanol three times and then drying for 12 h at 60 °C in the oven.

Structure characterizations: XRD patterns were obtained using a Rigaku diffractometer (DMAX-2500V/PC) with Cu-Kα (λ= 1.541 Å) source. The generator settings were 40 kV and 100 mA at the 2θ angle from 10° to 80°. The morphologies were observed by a scanning electron microscope (FE-SEM, Hitachi S-4800). TEM patterns were analyzed using an FE-TEM (Tecnai G2 F30ST). Raman spectroscopy was measured using the labRAM ARAMIS IR2 instrument. XPS was performed using the ULVAC-PHI instrument. Furthermore, UV-vis was tested using an Agilent Technologies (Cary 5000) instrument. TGA was tested in an Ar atmosphere with 10

°C/min heating rate. BET was analyzed using Tristar ll 3020 (Micromeritics, USA).

Electrochemical analysis: The electrochemical performance testing was performed using electrochemical workstations (Biologic SP-300) with a standard three-electrode system. The as-prepared catalyst was coated into a nickel foam as the working electrode with a size and loading of 1×1 cm^2 and approximately 5 mg/cm^2, respectively. Hg/HgO (saturated 1 M NaOH) electrode and Pt wire were used as reference and counter electrodes, respectively. We used 1.0 M KOH solutions as electrolytes. The values of all potentials shown in this study were based on the values of reversible hydrogen electrode (RHE) after calibration. The relationship between potential and RHE potential is E (RHE) = E (Hg/HgO) + 0.098 + 0.059 × pH, where E(RHE) is the potential referred to as RHE and E(Hg/HgO) denotes the measured potential against Hg/HgO (saturated KOH) reference electrode.

The polarization curves were measured by the LSV technique at 5 mV s^{-1} with 90% iR correction supported by the Biologic instrument. EIS was analyzed within a frequency range of 200 kHz–100 MHz in the 1.0 M KOH solution. The electrochemically active surface areas (ECSA) were determined from the double-layer capacitance (C_{dl}) measurements in the potential region of 0.8–0.9 V vs. RHE at different scan rates of 10, 20, 40, 60, 80, 100, and 120 mV/s. The relationship between ECSA and C_{dl} is $\mathrm{ECSA} = C_{dl}/C_s$, where, C_s is the specific capacitance value in 1M KOH.[S38]

Chronoamperometry was used to analyze the stability of electrocatalysts in electrochemical OER half-cell experiments.

The full-cell water splitting test was performed in the H-type equipment with CoO/CoP-NC as anode and cathode. LSV polarization curves were obtained at a scanning rate of 10 mV s^{-1} with 90% iR correction. Furthermore, current density-time testing of CoO/CoP-NC||CoO/CoP-NC was tested at 1.6 V and the volatage-time curve test was used to understand the stability of full-cell water splitting with the constant current density of 10 mA/cm^2 in a 1 M KOH solution.

DFT calculation: The first principles based on density functional theory (DFT) were calculated within the generalized gradient approximation using the Perdew-Burke-Ernzerhof formulation.[20] The projected augmented wave potentials were adopted to describe the ionic cores, and the kinetic energy cutoff was set at 400 eV for the plane wave function. The convergence threshold for the energy and force in all calculations was 10^{-4} eV and 0.02 eV/A, respectively. The vacuum height of over 15 Å on the z-axis was used to eliminate the interaction between adjacent periodic atoms. Moreover, the spin-polarization method was also considered in all electronic structure calculations. The 3×1×1 and 5×2×1 Γ-centered Monkhorst−Pack (MP) k-point grids were employed to sample the Brillion zone for the structural optimizations and electronic structure calculations. The dipole correction was used to compensate for the asymmetric layer arrangement; the van der Waals corrections (DFT-D3) were applied to describe the unbinding forces. The adsorption energies (E_{ads}) were calculated as

$$E_{ads} = E_{tot} - E_{sub} - E_{mol}, \qquad (1)$$

where E_{tot}, E_{sub}, and E_{mol} correspond to the total energies of the optimized adsorption system, the clean substrate, and the adsorbed molecule in the structure, respectively.[10, 20]

The variation in free energy (ΔG) for adsorbing H, OH, O, and OOH intermediates during the HER and OER processes was calculated by the following equation.

$$\Delta G = E_{ads} + \Delta E_{ZPE} - T\Delta S, \qquad (2)$$

where E_{ads} denotes the adsorption energy of the intermediate, ΔEZPE corresponds to the zero-point energy difference between the gaseous and adsorbed states, T is the temperature, and ΔS represents the change in entropy between the adsorbed and gaseous states. These values for adsorbed molecules were derived from NIST-JANAF thermochemical tables and high-quality literature. [S1, S2] Usually, the entropy variations of hydrogen adsorbed on the substrate surface is small. Therefore, the equation of the corrected free energy change is characterized as follows:

$$\Delta G = E_{ads} + 0.24\mathrm{eV} \qquad (3)$$

The OER process in an alkaline medium generally occurs through the following steps:

$$* + OH^- \rightarrow OH^* + e^- \qquad \Delta G1 \qquad (4)$$

$$OH^* + OH^- \rightarrow O^* + H_2O + e^- \qquad \Delta G2 \qquad (5)$$

$$O^* + OH^- \rightarrow OOH^* + e^- \qquad \Delta G3 \qquad (6)$$

$$OOH^* + OH^- \rightarrow O_2 + H_2O + e^- + * \qquad \Delta G4 \qquad (7)$$

where * denotes active adsorption site on the substrate.

$$\Delta G_1 = \Delta G_{OH} \qquad (8)$$

$$\Delta G_2 = \Delta G_O - \Delta G_{OH} \qquad (9)$$

$$\Delta G_3 = \Delta G_{OOH} - \Delta G_O \qquad (10)$$

$$\Delta G_4 = 4.92 - \Delta G_{OOH} \qquad (11)$$

The energy barrier η is defined as

$$\eta = \max\{\Delta G_1, \Delta G_2, \Delta G_3, \Delta G_4\} - 1.23\text{eV} \tag{12}$$

2. Figure and Table

Fig. S1. (a) The relaxed CoO (200) and **(b)** CoP (211) superpacket slab models. The blue, red, and pink spheres in the figure correspond to cobalt, oxygen, and phosphorus atoms, respectively.

Fig. S2. Planar-averaged electron density difference Δρ(z) for CoO/CoP heterostructure. The yellow and cyan areas indicate electron accumulation and depletion, respectively.

Fig. S3. Photographs of actual products of **(a)** $NaH_2PO_X \cdot xH_2O$ and **(b)** Co-precursor.

Fig. S4. XRD pattern of Co-precursor.

Fig. S5. TGA curve of Co-precursor.

Fig. S6. SEM image of Co-precursor.

Fig. S7. Morphology characterizations of as-prepared products. **(a–c)** SEM of CoO-NC and **(d–f)** SEM of CoP-NC.

Fig. S8. Element line scan for CoO/CoP-NC.

Fig. S9. (a) XRD patterns, **(b)** Raman spectra, and **(c, d)** UV-vis of as-prepared CoO-NC, CoP-NC, and CoO/CoP-NC heterostructures.

Fig. S10. XRD pattern under the ratio of Co-precursor and $NaH_2PO_2 \cdot {}_XH_2O$ with 1:0 (CoO-NC), 1:5 (CoO/CoP-NC (1:5)), 1:10 (CoO/CoP-NC), and 1:20 (CoO/CoP-NC (1:20)), respectively, at 350 °C for 2 h.

Fig. S11. N_2 adsorption/desorption isotherms of CoO-NC, CoP-NC, and CoO/CoP-NC, respectively.

Fig. S12. Magnified OER polarization curves for **Fig. 4. (d)**.

Fig. S13. (a) OER LSV curves at the ratio of Co-precursor and P-precursor with 1:0 (CoO-NC), 1:5 (CoO/CoP-NC (1:5)), 1:10 (CoO/CoP-NC) and 1:20 (CoO/CoP-NC (1:20)) under 350°C at 2 h. **(b)** The overpotential of 1:0, 1:5, 1:10, and 1:20 corresponding to LSV curves at 10, 50, and 100 mA cm^{-2}, respectively.

Fig. S14. (a) OER LSV curves of CoO/CoP-NC and Mixture COP-NC. **(b)** The overpotential of CoO/CoP-NC and Mixture COP-NC corresponding to LSV curves at 10, 50, and 100 mA cm^{-2}, respectively.

Fig. S15. Cyclic voltammograms (CV) of NF **(a)**, CoO-NC **(b)**, CoP-NC **(c)**, and CoO/CoP-NC **(d)** at different scan rates with 10, 20, 40, 60, 80, 100, and 120 mV/s in 1.0 M KOH.

Fig. S16. (a) The corresponding fitting plots C_{dl} of pristine NF, CoO-NC, CoP-NC, and CoO/CoP-NC, respectively. **(b)** Nyquist plots of pristine NF, CoO-NC, CoP-NC, and CoO/CoP-NC, respectively.

Fig. S17. Normalized LSV curves of NF, CoO-NC, CoP-NC, and CoO/CoP-NC by the electrochemical active surface area.

Fig. S18. The voltage-time testing of CoO/CoP-NC||CoO/CoP-NC at a constant current density (10 mA/cm^2).

Fig. S19. (a) SEM, **(b, c)** TEM, and **(d)** EDS-mapping of CoO/CoP-NC after OER long stability testing. XPS analysis of **(e)** Co 2p, **(f)** P 2p, and **(g)** O 1s for as-achieved target product, CoO/CoP-NC, before and after OER testing.

Fig. S20. **(a-f)** Theoretical structure models of **(a)** H adsorbed on CoO (200) facet (CoO (200)-H), **(b)** H adsorbed on CoP (211) facet (CoP (211)-H), **(c)** H adsorbed on CoO (200)/CoP (211) (CoO (200)/CoP (211)-H), **(d)** OH adsorbed on CoO (200)/CoP (211) (CoO (200)/CoP (211)-OH), **(e)** O adsorbed on CoO (200)/CoP (211) (CoO (200)/CoP (211)-O), and **(f)** OOH adsorbed on CoO (200)/CoP (211) (CoO (200)/CoP (211)-OOH).

Table S1. Element contents for XPS survey of CoO-NC, CoP-NC, and CoO/CoP-NC.

Table S3. Summary of various non-noble metal catalysts for an OER in 1.0 M KOH.

Table S4. Summary of various non-noble metal catalysts for HER in 1.0 M KOH.

Table S5. Bifunctional TMP-based heterostructure electrodes for efficient water splitting in 1M KOH.

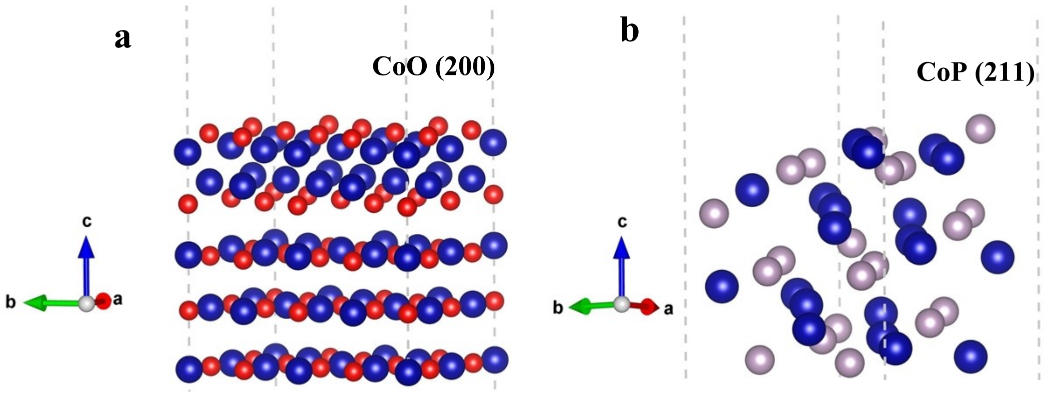

Fig. S1. (a) The relaxed CoO (200) and **(b)** CoP (211) superpacket slab models. The blue, red, and pink spheres in the figure correspond to cobalt, oxygen, and phosphorus atoms, respectively.

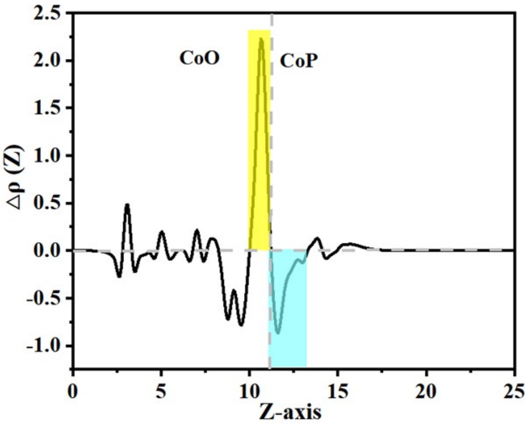

Fig. S2. Planar-averaged electron density difference Δρ(z) for CoO/CoP heterostructure. The yellow and cyan areas indicate electron accumulation and depletion, respectively.

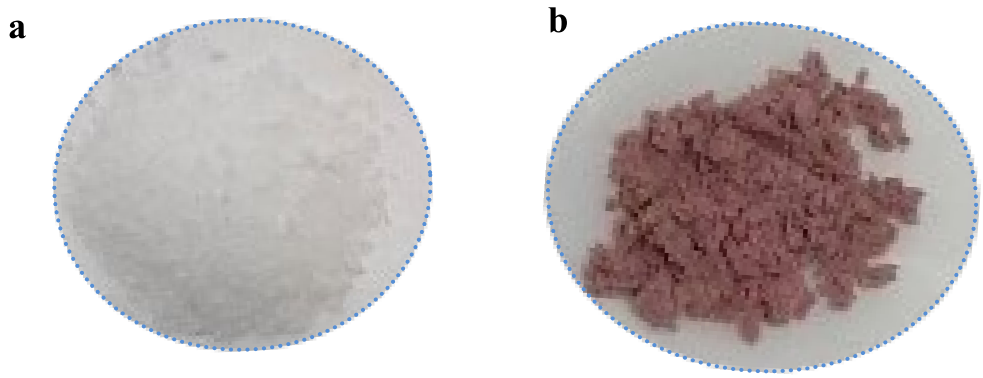

Fig. S3. Photographs of actual products of **(a)** $NaH_2PO_x \cdot xH_2O$ and **(b)** Co-precursor.

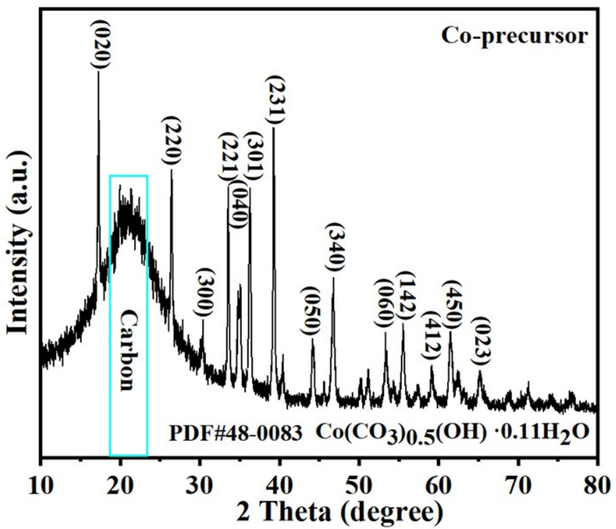

Fig. S4. XRD pattern of Co-precursor.

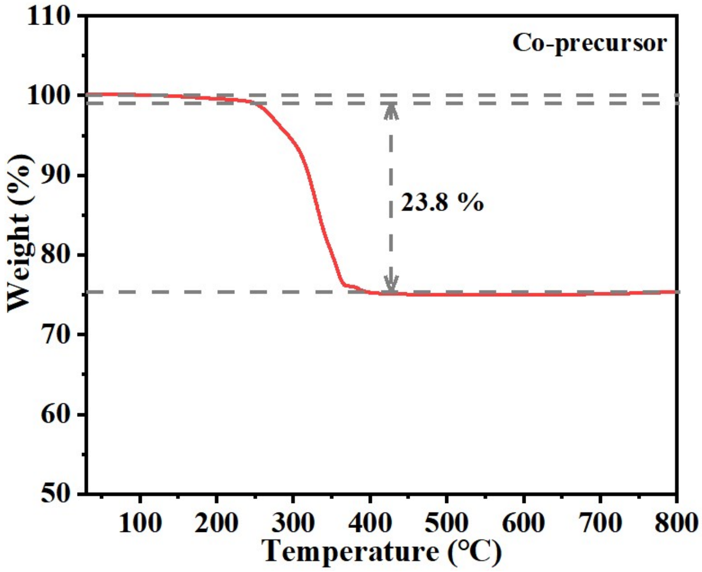

Fig. S5. TGA curve of Co-precursor.

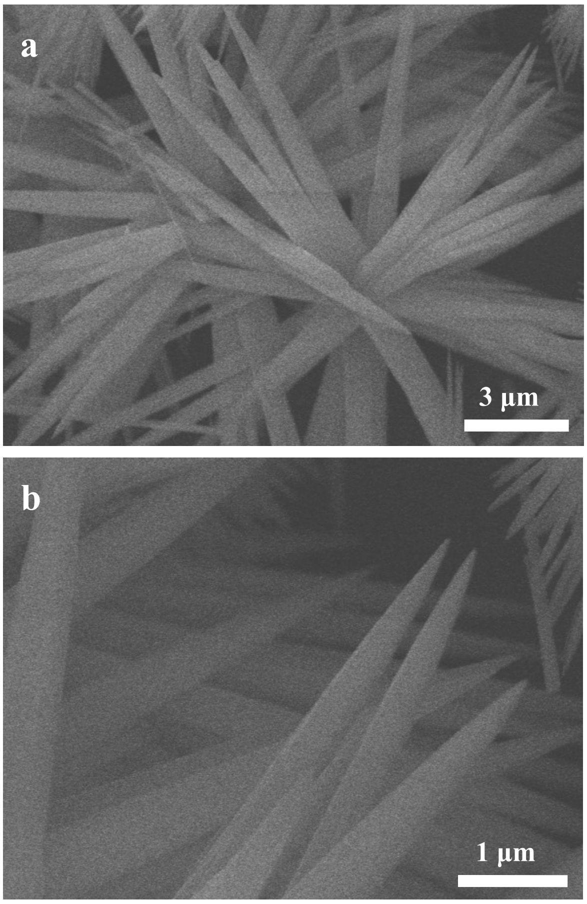

Fig. S6. SEM image of Co-precursor.

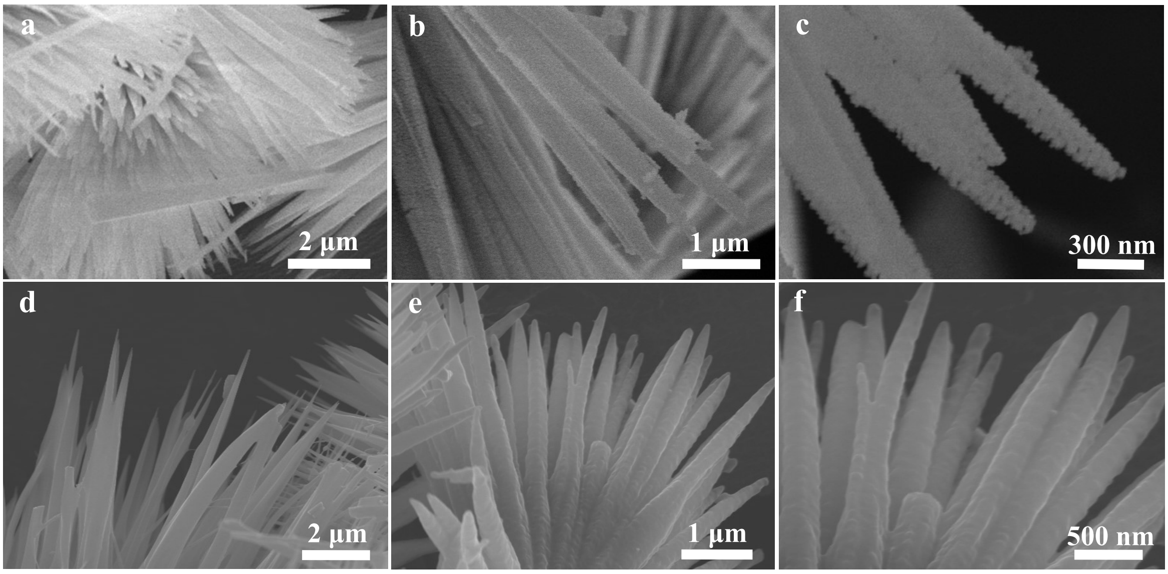

Fig. S7. Morphology characterizations of as-prepared products. **(a–c)** SEM of CoO-NC and **(d–f)** SEM of CoP-NC.

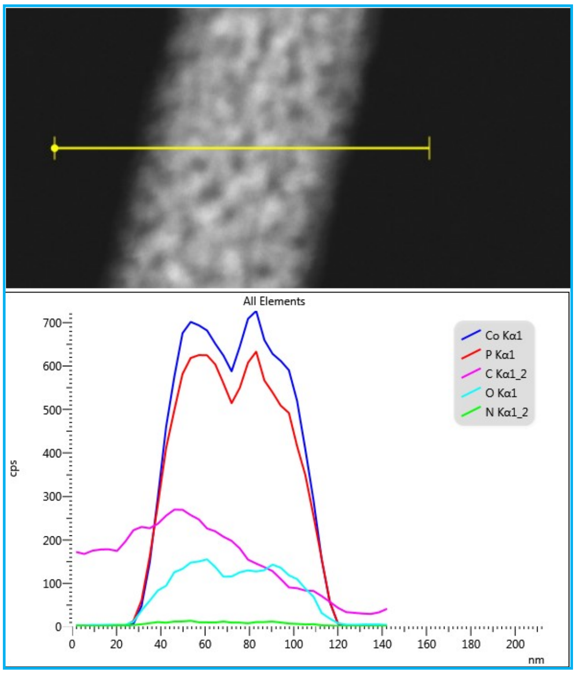

Fig. S8. Element line scan for CoO/CoP-NC.

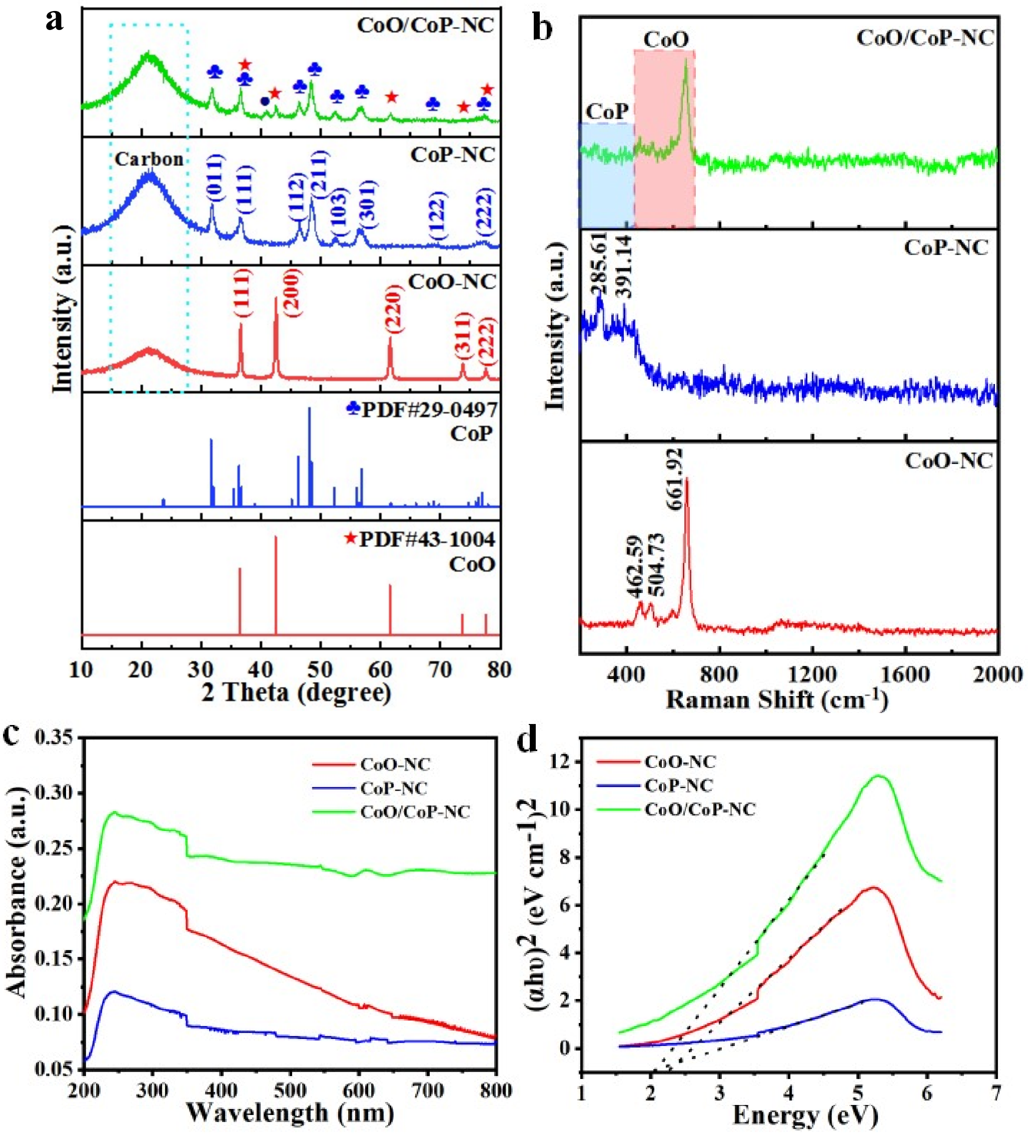

Fig. S9. (a) XRD patterns, **(b)** Raman spectra, and **(c, d)** UV-vis of as-prepared CoO-NC, CoP-NC, and CoO/CoP-NC heterostructures.

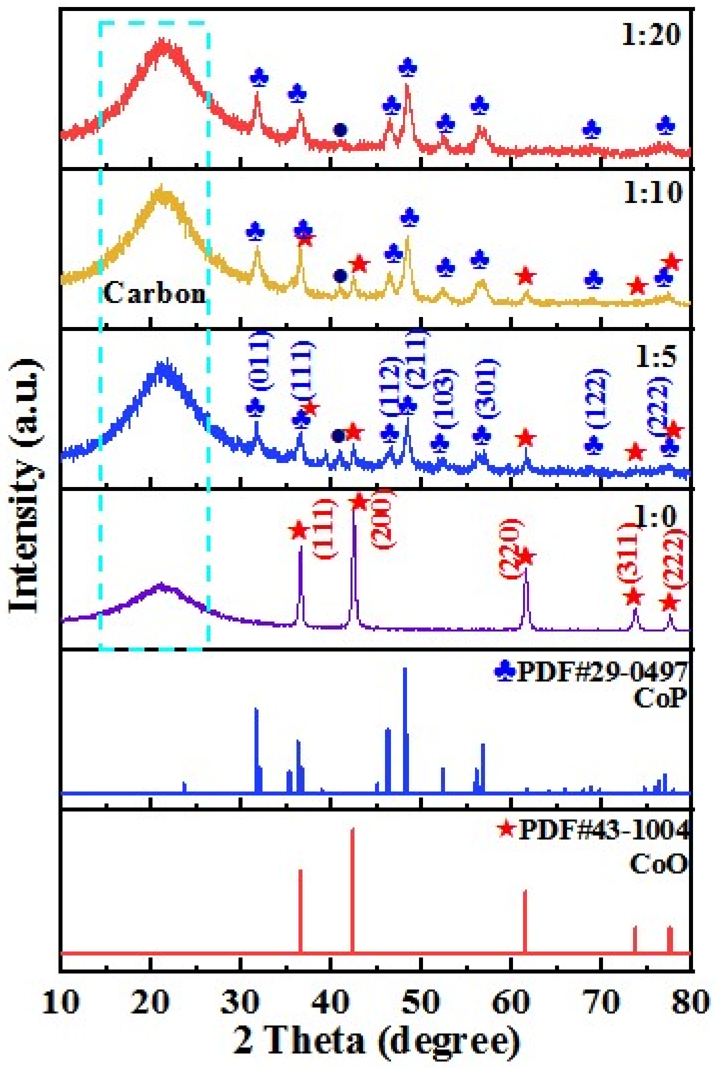

Fig. S10. XRD pattern under the ratio of Co-precursor and $NaH_2PO_2{\cdot}_XH_2O$ with 1:0 (CoO-NC), 1:5 (CoO/CoP-NC (1:5)), 1:10 (CoO/CoP-NC), and 1:20 (CoO/CoP-NC (1:20)), respectively, at 350 °C for 2 h.

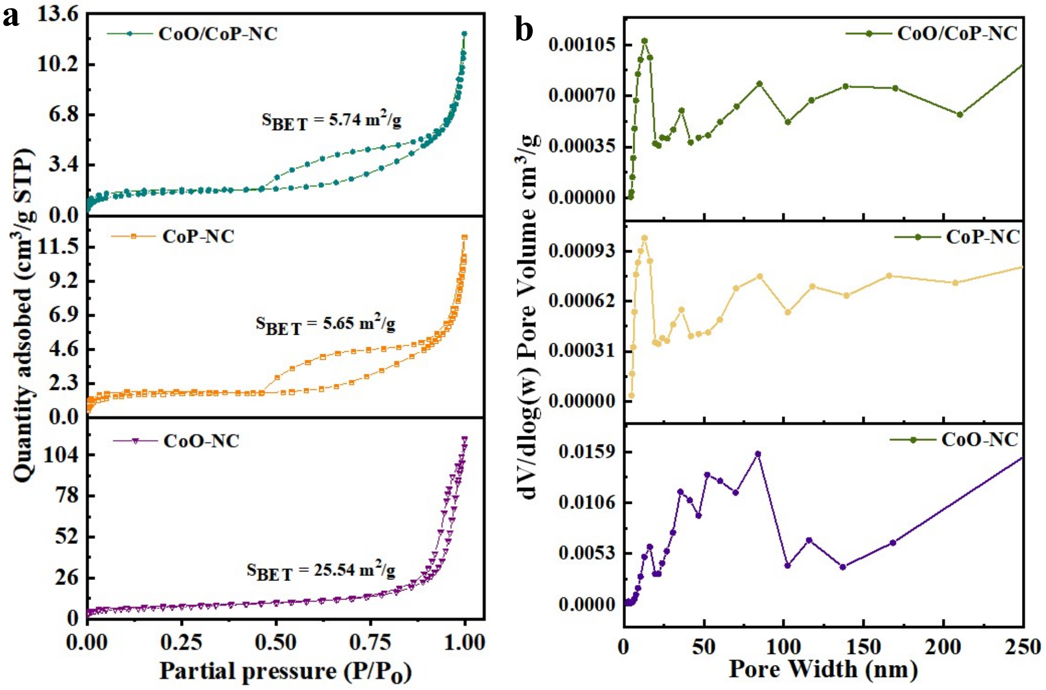

Fig. S11. (a) N_2 adsorption/desorption isotherms of CoO-NC, CoP-NC, and CoO/CoP-NC, respectively. **(b)** The pore size distribution curves of CoO-NC, CoP-NC, and CoO/CoP-NC, respectively.

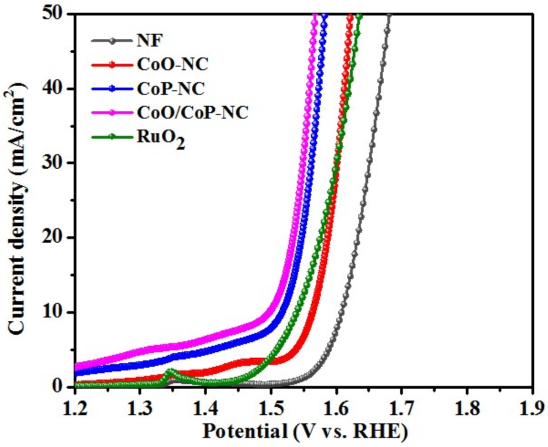

Fig. S12. Magnified OER polarization curves for **Fig. 4. (d)**.

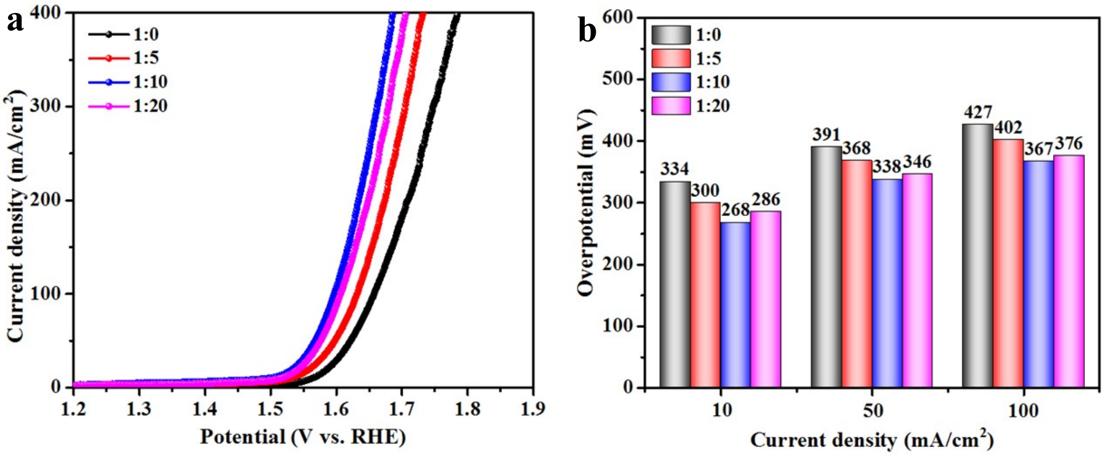

Fig. S13. (a) OER LSV curves at the ratio of Co-precursor and P-precursor with 1:0 (CoO-NC), 1:5 (CoO/CoP-NC (1:5)), 1:10 (CoO/CoP-NC) and 1:20 (CoO/CoP-NC (1:20)) under 350°C at 2 h. **(b)** The overpotential of 1:0, 1:5, 1:10, and 1:20 corresponding to LSV curves at 10, 50, and 100 mA cm^{-2}, respectively.

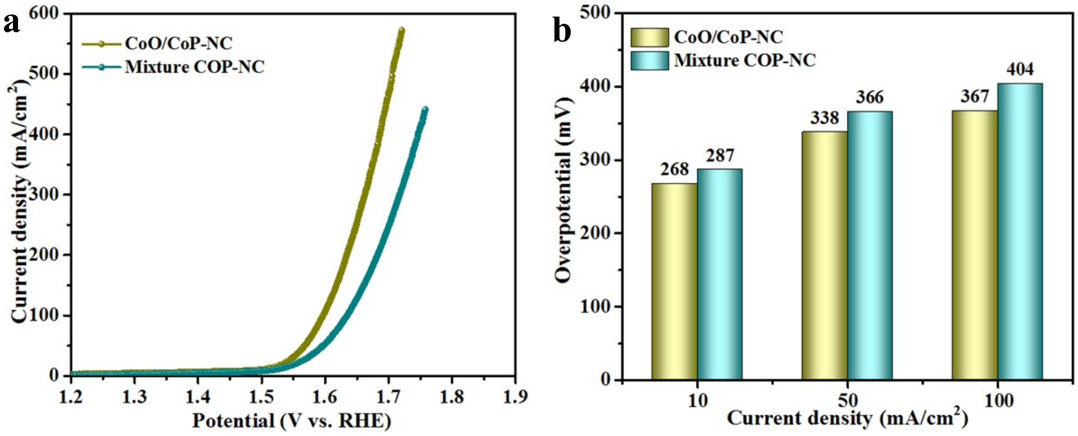

Fig. S14. (a) OER LSV curves of CoO/CoP-NC and Mixture COP-NC. **(b)** The overpotential of CoO/CoP-NC and Mixture COP-NC corresponding to LSV curves at 10, 50, and 100 mA cm^{-2}, respectively.

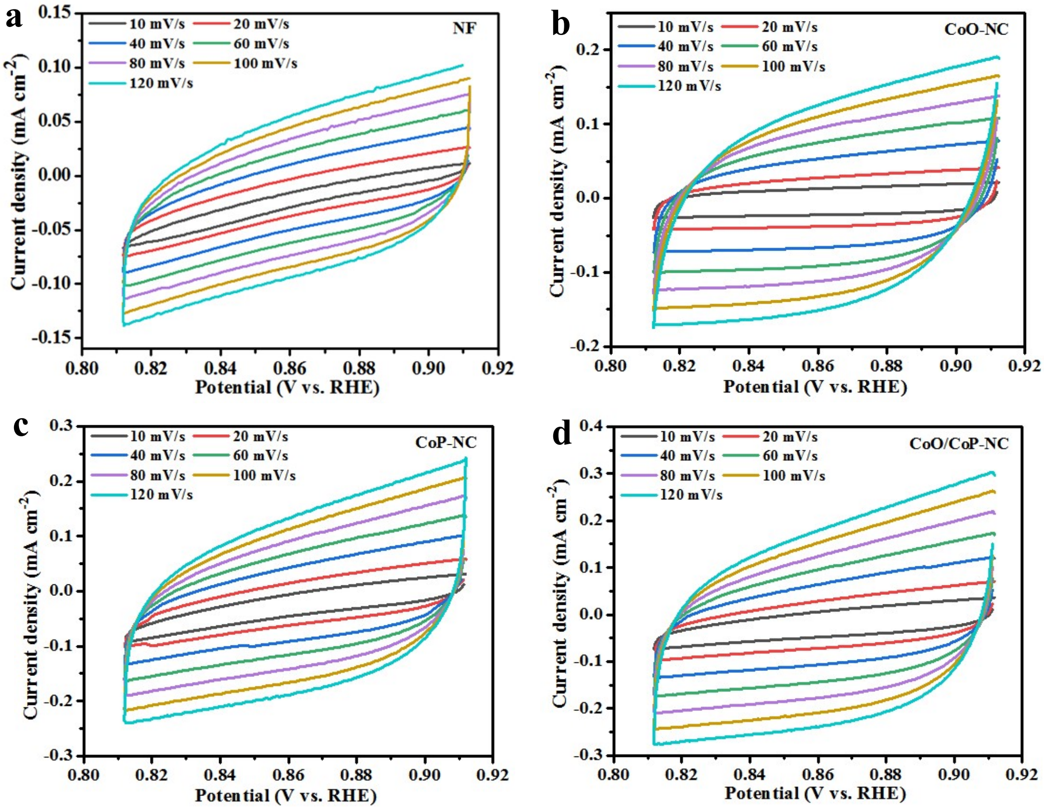

Fig. S15. Cyclic voltammograms (CV) of NF **(a)**, CoO-NC **(b)**, CoP-NC **(c)**, and CoO/CoP-NC **(d)** at different scan rates with 10, 20, 40, 60, 80, 100, and 120 mV/s in 1.0 M KOH.

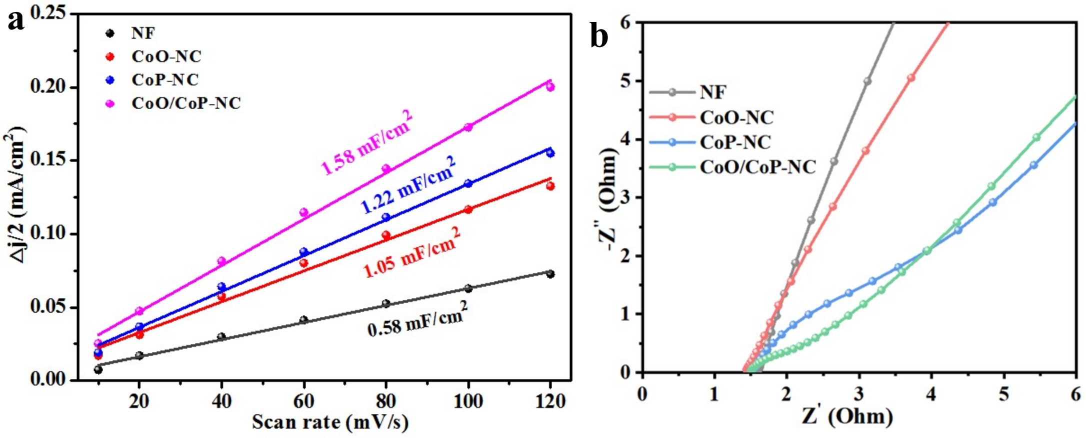

Fig. S16. (a) The corresponding fitting plots C_{dl} of pristine NF, CoO-NC, CoP-NC, and CoO/CoP-NC, respectively. **(b)** Nyquist plots of pristine NF, CoO-NC, CoP-NC, and CoO/CoP-NC, respectively.

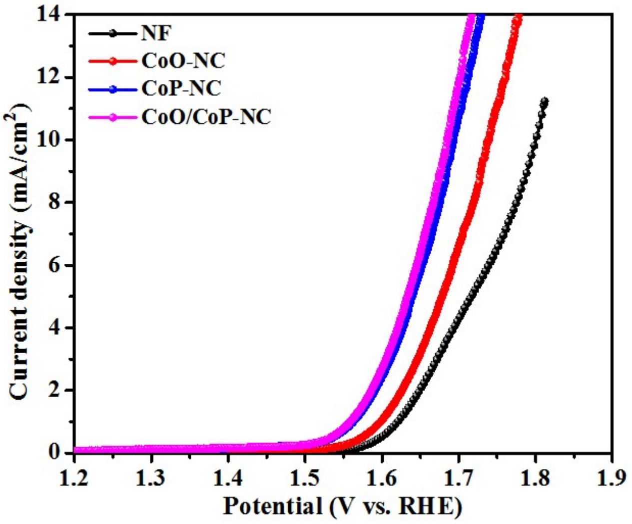

Fig. S17. Normalized LSV curves of NF, CoO-NC, CoP-NC, and CoO/CoP-NC by the electrochemical active surface area.

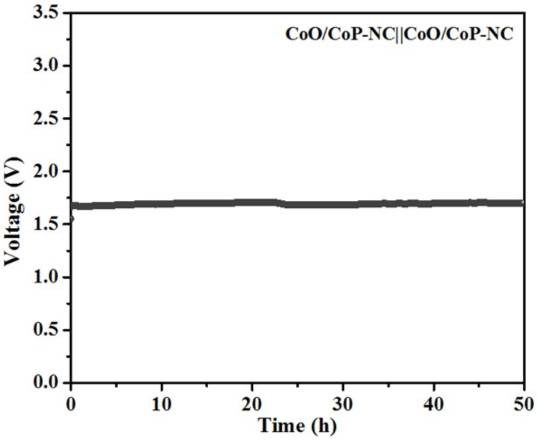

Fig. S18. The voltage-time testing of CoO/CoP-NC||CoO/CoP-NC at a constant current density (10 mA/cm^2).

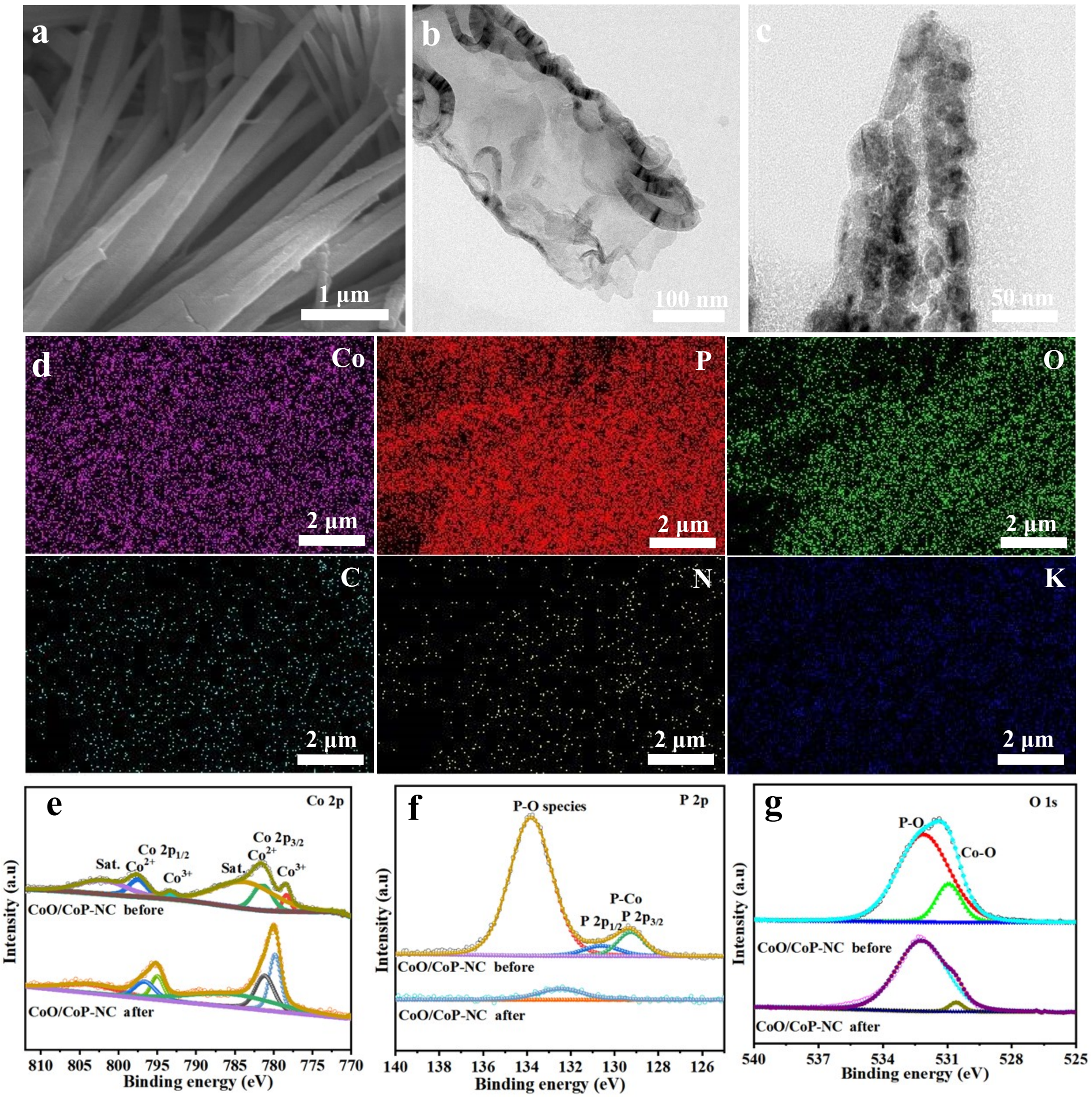

Fig. S19. (a) SEM, **(b, c)** TEM, and **(d)** EDS-mapping of CoO/CoP-NC after OER long stability testing. XPS analysis of **(e)** Co 2p, **(f)** P 2p, and **(g)** O 1s for as-achieved target product CoO/CoP-NC before and after OER testing.

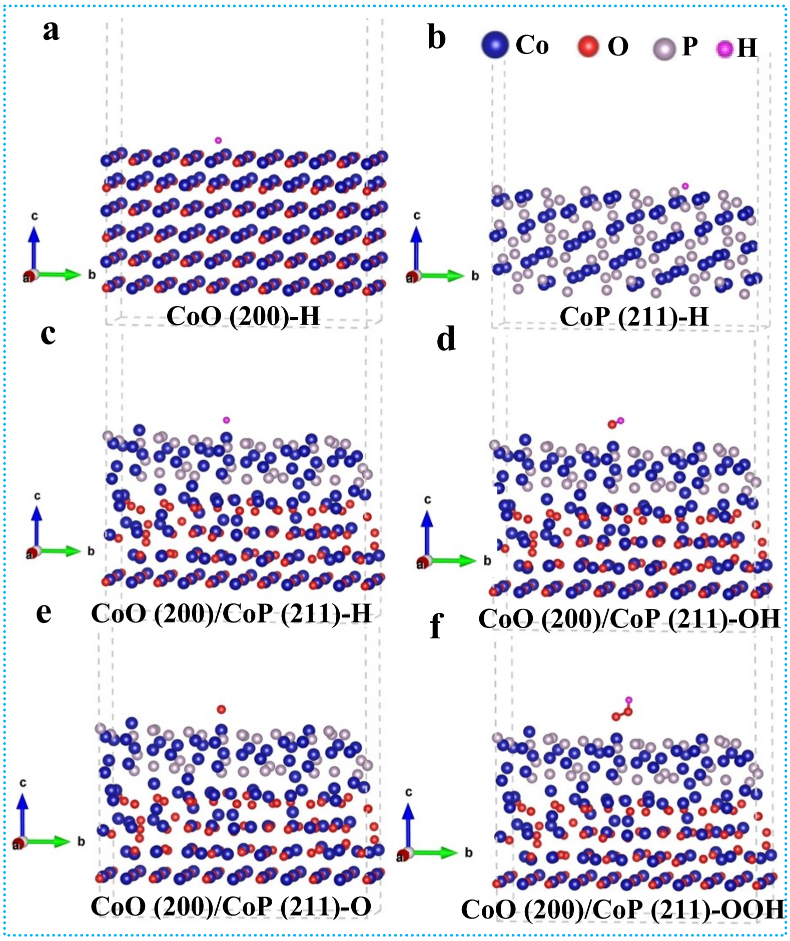

Fig. S20. (a-f) Theoretical structure models of **(a)** H adsorbed on CoO (200) facet (CoO (200)-H), **(b)** H adsorbed on CoP (211) facet (CoP (211)-H), **(c)** H adsorbed on CoO (200)/CoP (211) (CoO (200)/CoP (211)-H), **(d)** OH adsorbed on CoO (200)/CoP (211) (CoO (200)/CoP (211)-OH), **(e)** O adsorbed on CoO (200)/CoP (211) (CoO (200)/CoP (211)-O), and **(f)** OOH adsorbed on CoO (200)/CoP (211) (CoO (200)/CoP (211)-OOH).

Table S1. Element contents for XPS survey of CoO-NC, CoP-NC, and CoO/CoP-NC.

Catalysts	Elements	Atoms (at%)
CoO-NC	Co 2p	31.4
	O 1s	41.0
	P 2p	<0.1
	C 1s	27.6
	N 1s	<0.1
CoP-NC	Co 2p	13.2
	O 1s	58.1
	P 2p	13.2
	C 1s	9.9
	N 1s	1.5
CoO/CoP-NC	Co 2p	11.3
	O 1s	59.6
	P 2p	18.3
	C 1s	9.5
	N 1s	1.3

Table S2. Summary of various non-noble metal catalysts for an OER in 1.0 M KOH.

Catalysts	**Overpotential (mV, at 10 mA/cm^2)**	**Tafel slope (mV/dec)**	**electrolyte**	**Ref.**
CoO/CoP-NC	**268**	**90**	**1 M KOH**	**This work**
Co/CNT/MCP-850	270	79	1 M KOH	[S3]
Co/CNFs (1000)	320	79	1 M KOH	[S4]
CoP−FeP/CC	250	131	1 M KOH	[S5]
NiCoP/C nanoboxes	330	96	1 M KOH	[S6]
CoP NP/C	320	71	1 M KOH	[S7]
CoP-CoO/CC	210	90	1 M KOH	[S8]
CoOx@CN	260	--	1 M KOH	[S9]
Co_6W_6C@NC/CC	286	53.96	1 M KOH	[S10]
$CuCo_2S_4$	310	86	1 M KOH	[S11]
W_2N/WC	320	94.5	1 M KOH	[S12]

Table S3. Summary of various non-noble metal catalysts for HER in 1.0 M KOH.

Catalysts	**Overpotential (mV, at -10 mA/cm^2)**	**Tafel slope**	**electrolyte**	**Ref.**
CoO/CoP-NC	**178**	**88**	**1 M KOH**	**This work**
Fe_3C-Co/NC	238	108.8	1 M KOH	[S13]
CF–NG–Co	212	75	1 M KOH	[S14]
Co_2P/NPG-900	245	108.6	1 M KOH	[S15]
CoWCP-NPC-2:1 CoWCP-NPC-1:1	139 217	116.9 175.3	1 M KOH	[S16]
1% Co-N-GDY	271	132	1 M KOH	[S17]
Fe_3Co_7@PCNSs	205	65.5	1 M KOH	[S18]
CoP/CC	209	129	1 M KOH	[S19]
CoNi-OOH-30(40)	210	67	1 M KOH	[S20]
CoP/NiCoP NTs	133	88	1 M KOH	[S21]
MoS_2@Co_3S_4	210	88	1 M KOH	[S22]

Table S4. Bifunctional TMP-based heterostructure electrodes for efficient water splitting in 1M KOH.

Catalysts	Substrate	Current density	Voltage for overall	Electrolyte	Ref.
CoO/CoP-NC	**Nickel foam**	**10 mA/cm^2**	**1.53 V**	**1 M KOH**	**This work**
$P_{8.6}$-Co_3O_4/NF	Nickel foam	10 mA/cm^2	1.63 V	1 M KOH	[S23]
Er-doped CoP NMs	Carbon cloth	10 mA/cm^2	1.58 V	1 M KOH	[S24]
O-CoP	Nickel foam	10 mA/cm^2	1.60 V	1 M KOH	[S25]
Cu-CoP NAs/CP	Carbon paper	10 mA/cm^2	1.72 V	1 M PBS	[S26]
CoP–N/Co foam	Co foam	50 mA/cm^2	1.61 V	1 M KOH	[S27]
B,N,S-CoP@C@rGO	Carbon paper	10 mA/cm^2	1.50 V	1 M KOH	[S28]
Ni-CoP-5%	Carbon paper	10 mA/cm^2	1.56 V	1 M KOH	[S29]
CoP-NC@NFP	Nickel foam	10 mA/cm^2	1.57 V	1 M KOH	[S30]
Co/CoP@HOMC	Glassy carbon	10 mA/cm^2	1.54 V	1 M KOH	[S31]
V-CoP@ a-CeO_2	Carbon cloth	10 mA/cm^2	1.56 V	1 M KOH	[S32]
V-CoP	Nickel foam	10 mA/cm^2	1.59 V	1 M KOH	[S33]
Co_2P/CoP@Co@NCNT	Carbon cloth	10 mA/cm^2	1.60 V	1 M KOH	[S34]
CP	Nickel foam	10 mA/cm^2	1.498V	1 M KOH	[S35]
CoP@FeCoP/NC YSMPs	Carbon paper	10 mA/cm^2	1.68 V	1 M KOH	[S36]
CoP NB	Carbon paper	10 mA/cm^2	1.58 V	1 M KOH	[S37]

Reference

S1 NIST-JANAF Thermochemical Tables. https://janaf.nist.gov/.

S2 P. L. Zhai, Y. X. Zhang, Y. Z. Wu, J. F. Gao, B. Zhang, S. Y. Cao, Y. T. Zhang, Z. W. Li, L. C. Sun, J. G. Hou, *Nat. Commun.*, 2020, **11**, 5462.

S3 X. W. Zhou, X. Liu, J. H. Zhang, C. Zhang, S. J. Yoo, J. G. Kim, X. Y. Chu, C. Song, P. Wang, Z. Z. Zhao, D. B. Li, W. Zhang, W. T. Zheng, *Carbon*, 2020, **166**, 284–290.

S4 Z. K. Yang, C. M. Zhao, Y. T. Qu, H. Zhou, F. Y. Zhou, J. Wang, Y. E. Wu, Y. D. Li, *Adv. Mater.*, 2019, **31**, 1808043.

S5 Z. G. Niu, C. Qiu, J. Jiang, L. H. Ai, *ACS Sustain. Chem. Eng.*, 2019, **7**, 2335–2342.

S6 P. L. He, X. Y. Yu, X. W. (David) Lou, *Angew. Chem. Int. Ed.*, 2017, **56**, 3897–3900.

S7 J. F. Chang, Y. Xiao, M. L. Xiao, J. J. Ge, C. P. Liu, W. Xing, *ACS Catal.*, 2015, **5**, 6874–6878.

S8 J. Yao, M. Y. Zhang, X. Z. Ma, L. L. Xu, F. Gao, J. P. Xiao, H. Gao, *J. Colloid Interface Sci.*, 2022, **607**, 1343–1352.

S9 H. Y. Jin, J. Wang, D. F. Su, Z. Z. Wei, Z. F. Pang, Y. Wang, *J. Am. Chem. Soc.*, 2015, **137**, 2688–2694.

S10 J. P. Chen, B. W. Ren, H. Cui, C. X. Wang, *Small*, 2020, **16**, 1907556.

S11 M. Chauhan, K. P. Reddy, C. S. Gopinath, S. Deka, *ACS Catal.*, 2017, **7**, 5871–5879.

S12 J. X. Diao, Y. Qiu, S. Q. Liu, W. T. Wang, K. Chen, H. L. Li, W. Y. Yuan, Y. T. Qu, X. H. Guo, *Adv. Mater.*, 2020, **32**, 1905679.

S13 C. C. Yang, S. F. Zai, Y. T. Zhou, L. Du, Q. Jiang, *Adv. Funct. Mater.*, 2019, **29**, 1901949.

S14 Z. X. Pei, Z. J. Tang, Z. X. Liu, Y. Huang, Y. K. Wang, H. F. Li, Q. Xue, M. S. Zhu, D. M.

Tang, C. Y. Zhi, *J. Mater. Chem. A*, 2018, **6**, 489–497.

S15 Q. Shao, Y. Li, X. Cui, T. J. Li, H. G. Wang, Y. H. Li, Q. Duan, Z. J. Si, *ACS Sustain. Chem. Eng.*, 2020, **8**, 6422−6432.

S16 Y. N. Zhang, W. P. Shi, L. L. Bo, Y. X. Shen, X. C. Ji, L. C. Xia, X. L. Guan, Y. X. Wang, J. H. Tong, *Chem. Eng. J.*, 2022, **431**, 134188.

S17 X. Wang, Z. Yang, W. Y. Si, X. Y. Shen, X. D. Li, R. Li, Q. Lv, N. Wang, C. S. Huang, *Carbon*, 2019, **147**, 9−18.

S18 T. T. Liu, M. Li, X. J. Bo, M. Zhou, *J. Colloid Interface Sci.*, 2019, **537**, 280−294.

S19 J. Q. Tian, Q. Liu, A. M. Asiri, X. P. Sun, *J. Am. Chem. Soc.*, 2014, **136**, 7587−7590.

S20 C. Yu, J. J. Lu, L. Luo, F. Xu, P. K. Shen, P. Tsiakaras, S. B. Yin, *Electrochimica Acta*, 2019, **301**, 449−457.

S21 Y. Lin, K. A. Sun, S. J. Liu, X. M. Chen, Y. S. Cheng, W. C. Cheong, Z. Chen, L. R. Zheng, J. Zhang, X. Y. Li, Y. Pan, C. Chen, Adv. Energy Mater., 2019, **9**, 1901213.

S22 S. Dutta, Z. M. Liu, H. S. Han, A. Indra, T. Song, *ChemElectroChem*, 2018, **5**, 3571–3588.

S23 Z. C. Wang, H. L. Liu, R. X. Ge, X. Ren, J. Ren, D. J. Yang, L. X. Zhang, X. P. Sun, *ACS Catal.*, 2018, **8**, 2236−2241.

S24 G. W. Zhang, B. Wang, J. L. Bi, D. Q. Fang, S. C. Yang, *J. Mater. Chem. A*, 2019, **7**, 5769−5778.

S25 G. Y. Zhou, M. Li, Y. L. Li, H. Dong, D. M. Sun, X. E. Liu, L. Xu, Z. Q. Tian, Y. W. Tang, *Adv. Funct. Mater.*, 2020, **30**, 1905252.

S26 L. Yan, B. Zhang, J. L. Zhu, Y. Y. Li, P. Tsiakaras, P. K. Shen, *Appl. Catal. B: Environ.*, 2020, **265**, 118555.

S27 Z. Liu, X. Yu, H. G. Xue, L. G. Feng, *J. Mater. Chem. A*, 2019, **7**, 13242−13248.

S28 H. B. Xu, H. X. Jia, B. Fei, Y. Ha, H. Z. Li, Y. H. Guo, M. Liu, R. B. Wu, *Appl. Catal. B: Environ.*, 2020, **268**, 118404.

S29 Y. F. Zhao, J. Q. Zhang, Y. H. Xie, B. Sun, J. J. Jiang, W. J. Jiang, S. B. Xi, H. Y. Yang, K. Yan, S. J. Wang, X. Guo, P. Li, Z. J. Han, X. Y. Lu, H. Liu, G. X. Wang, *Nano Lett.*, 2021, **21**, 823−832.

S30 E. Vijayakumar, S. Ramakrishnan, C. Sathiskumar, D. J. Yoo, J. Balamurugan, H. S. Noh, D. Kwon, Y. H. Kim, H. G. Lee, *Chem. Eng. J.*, 2022, **428**, 131115.

S31 W. Li, J. Liu, P. F. Guo, H. Z. Li, B. Fei, Y. H. Guo, H. G. Pan, D. L. Sun, F. Fang, R. B. Wu, *Adv. Energy Mater.*, 2021, **11**, 2102134.

S32 L. Yang, R. M. Liu, L. F. Jiao, *Adv. Funct. Mater.*, 2020, **30**, 1909618.

S33 R. Zhang, Z. H. Wei, G. Y. Ye, G. J. Chen, J. J. Miao, X. H. Zhou, X. W. Zhu, X. Q. Cao, X. N. Sun, *Adv. Energy Mater.*, 2021, **11**, 2101758.

S34 Z. J. Lu, Y. L. Cao, J. Xie, J. D. Hu, K. Wang, D. Z. Jia, *Chem. Eng. J.*, 2022, **430**, 132877.

S35 D. W. Kim, X. Y. Qin, B. Y. Yan, Y. Z. Piao, *Chem. Eng. J.*, 2021, **408**, 127331.

S36 J. H. Shi, F. Qiu, W. B. Yuan, M. M. Guo, Z. H. Lu, *Chem. Eng. J.*, 2021, **403**, 126312.

S37 L. Yan, S. Z. Zhao, Y. Y. Li, B. Zhang, J. L. Zhu, Z. G. Liu, X. X. Yuan, J. L. Yu, H. Y. Zhang, P. K. Shen, *Mater. Today Energy*, 2019, **12**, 443−452.

S38 S. Singh, D. C. Nguyen, N. H. Kim, J. H. Lee, *Chem. Eng. J.*, 2022, **442**, 136120.